

# Microwave Flexible Electronics Directly Transformed from Foundry-Produced, Multilayered Monolithic Integrated Circuits

Guoxuan Qin, Yei Hwan Jung, Huilong Zhang, Ningyue Jiang, Pingxi Ma, Scott Stetson, Marco Racanelli, and Zhenqiang Ma\*

Monolithic microwave integrated circuits hold a dominant position in telecom applications, especially in mobile devices with capabilities for wireless connectivity, due to high and repeatable performance, compact form factor, and low cost. With flexible electronic technologies forming the foundation for a rapidly growing wearable and implantable device segment, the need for flexible microwave electronics with levels of performance that match those of rigid counterparts has increased to unprecedented levels. Here, the fabrication processes for transforming a rigid form of foundry-produced, multilayered monolithic microwave integrated circuit into a flexible format for amplification of radio frequency signals in the gigahertz level are described. The strategy involves a complete replacement of all rigid materials in the integrated circuit that do not provide any active electronic functionality with a soft, silicone elastomer to yield an overall structure that is mechanically compliant. Experimental studies indicate that the transformation process leads to a flexible silicon-germanium-based heterojunction bipolar transistor with a maximum oscillation frequency of 49 GHz and a 24 GHz amplifier with a small-signal gain of 13.2 dB. This approach has potential uses across a diverse set of microwave devices and circuits, in a manner that could enable wireless connectivity using entirely flexible electronics.

## 1. Introduction

The rapid pace of innovation in flexible electronics enables a range of new applications that are inaccessible by conventional rigid substrate-based counterparts, such as flexible displays, biomedical devices, and curvilinear image sensors.<sup>[1–6]</sup> The emerging era of big data and internet-of-things demands wireless connectivity in these applications, requiring radio-frequency (RF) integrated circuits (IC) for amplification, mixing, and switching of microwave signals.<sup>[7]</sup> Despite the encouraging advances in flexible components, unfortunately, at present, these developments have not reached the electrical performance levels that match those of conventional electronic components, especially the microwave ICs.<sup>[8]</sup> Thus, existing flexible electronics connect to external circuit boards, often in hybrid forms that solder rigid conventional ICs on flexible printed circuit boards, to achieve advanced pro-

cessing and amplification required for wireless communication, resulting in partially flexible devices that only bends at the component-free regions.<sup>[9,10]</sup> An objective is to eliminate such rigid regions by replacing them with flexible ICs that house transistors and passive elements for enabling advanced microwave functions analogous to rigid chips that drive wireless operations in mobile electronic devices.

Developing a flexible microwave IC that matches the performance criteria of state-of-the-art ICs poses a number of technical challenges.<sup>[11,12]</sup> Organic semiconductors cannot satisfy the high-performance requirements of conventional ICs, due to their intrinsically low carrier mobility characteristics.<sup>[13]</sup> Novel 2D semiconductors like graphene and molybdenum disulfide show promising research direction toward high-performance flexible ICs, but they require verifications of reliability and reproducibility for successful commercialization.<sup>[14]</sup> Printing inorganic micro- or nano-membranes obtained from single-crystal wafers on foreign substrates demonstrates to be the most viable approach as these thin films preserve the high carrier mobility characteristics of wafer-based semiconductors. However, the existing fabrication approach prohibits the downscaling of critical dimensions with high alignment

G. Qin, H. Zhang, N. Jiang, Z. Ma  
Department of Electrical and Computer Engineering  
University of Wisconsin–Madison  
Madison, WI 53706, USA  
E-mail: mazq@engr.wisc.edu

G. Qin  
School of Microelectronics  
Tianjin University  
Tianjin 300072, P. R. China

Y. H. Jung  
Department of Electronic Engineering  
Hanyang University  
Seoul 04763, Republic of Korea

P. Ma, S. Stetson, M. Racanelli  
Jazz Semiconductor, Inc.  
Newport Beach, CA 9660, USA

 The ORCID identification number(s) for the author(s) of this article can be found under <https://doi.org/10.1002/aelm.202101350>.

© 2022 The Authors. Advanced Electronic Materials published by Wiley-VCH GmbH. This is an open access article under the terms of the Creative Commons Attribution-NonCommercial License, which permits use, distribution and reproduction in any medium, provided the original work is properly cited and is not used for commercial purposes.

DOI: 10.1002/aelm.202101350

precision (e.g., between gate and source/drain) on plastics or rubber sheets (soft and stretchable) for enhancing device performance.<sup>[15]</sup> An approach to overcome such limitation assembles a foundry-produced, fully formed set of thin-film, inorganic devices on flexible substrates into an organized array for stable, high-performance operation, with examples ranging from silicon (Si)-based metal-oxide-semiconductor field effect devices for logic gates and gallium nitride-based high electron mobility transistors for microwave amplifiers.<sup>[16–18]</sup> Although many important ICs can be achieved with this approach, such discrete format limits size reduction of the overall IC, due in part by the minimum distance requirement between each transfer-printed fully formed device. In comparison, a conventional IC monolithically integrates transistors and passive components on a single piece of semiconductor connected via multiple metal layers, bringing each element in close proximity and reducing the overall size, thereby increasing speed and lowering power consumption.<sup>[19]</sup> The challenge of using discrete components can be more prominent in microwave ICs as multilayers of high-frequency components require matching at specific characteristic impedances (mostly 50  $\Omega$  environment) and precise alignment to account for any parasitic and stray capacitance and inductance exhibited in each component. In particular, the densely packed multilayer metal interconnections, which are crucial for advanced ICs, present an inevitable obstacle to fabricate extremely flexible and high-frequency electronics using transfer printing techniques.

An alternate and conceptually different approach obtains flexible ICs through mechanical exfoliation or etching of carrier substrates from conventional wafer-based systems to preserve the crystallinity and characteristics of the high-performance active circuit layers.<sup>[20–22]</sup> The relatively large area and brittleness of the active layers cannot avoid crack formations across the surface under extreme bending. The brittleness mainly arises from the multilayered oxide-based dielectric layers present between multilevel interconnects. Here, we introduce a fabrication strategy to transform conventional rigid chip-based monolithic microwave IC (MMIC) interconnected with multilayer electrical traces of metal into a flexible format while preserving its high-frequency performance. The method completely removes the carrier substrate as well as all the oxide layers that are present in between multilayers, leaving behind only the active electronic devices and interconnects, which we call the “skeleton” of the IC. The approach can be used to transform a foundry-produced, multilayer millimeter-wave silicon-germanium (SiGe) heterojunction bipolar transistor (HBT)-based small-signal amplifier into a flexible and robust chip that completely maintains its high-frequency response characteristics. Individual analysis of the flexible HBTs and passive components achieved in this manner shows little performance degradation after the transformation process. The transistor current gain, high-frequency unilateral gain, and other characteristics of HBT achieved in a flexible format using this technique exceed those of any previous similar demonstrations. Careful comparisons of the electrical characteristics for different conditions of oxide removal processes reveal the optimal fabrication strategy for transforming rigid to flexible IC. Further, a stretchable elastomer-based dielectric material replaces all voided areas created from the oxide removal process, thereby maintaining

stable insulation between layers and yielding a robust operation under various mechanically deformed conditions. The electrical and mechanical performances achieved with this set of attributes indicate that the approach is suitable for transforming a conventional IC to a flexible form.

## 2. Results and Discussion

The work presented here employs a commercial two-stage small-signal amplifier (24 GHz) that consists of 5 and 16 SiGe HBTs at the first stage and second stage, respectively, based on the 0.18  $\mu\text{m}$  SiGe90 process technology from Jazz Semiconductor Inc. Each HBT contains four emitter fingers with dimensions of  $0.2 \times 10.16 \mu\text{m}^2$  for each finger. The completed chip includes four aluminum layers (2  $\mu\text{m}$  thick) separated with intermetal dielectric (IMD; 2.5  $\mu\text{m}$  thick) and an interlayer dielectric (ILD; 2.5  $\mu\text{m}$  thick; planarized) layers of  $\text{SiO}_2$ . Capacitors that are based on metal–insulator ( $\text{Ta}_2\text{O}_5$ )–metal (MIM) structures and inductors that are based on spiral shapes sit in between the IMD layers, which connect to the HBTs that lie beneath the ILD layer. The entire stack sits on top of a graded  $\text{Si}_{1-x}\text{Ge}_x$  (13  $\mu\text{m}$  thick) layer grown from an undoped Si handling wafer (600  $\mu\text{m}$  thick).

The schematic illustrations in **Figure 1a–e** present the fabrication steps for transforming foundry-produced microwave devices and ICs with multilayer metal interconnections into flexible formats. As illustrated in **Figure 1b**, the first procedure involves the removal of the oxide layers using combinations of reactive ion etching (RIE) and wet chemical etching, starting with an RIE using halocarbon-14 ( $\text{CF}_4$ ) gas to remove the top exposed layer, followed by hydrofluoric (HF) acid-based wet etching to remove the IMD layers. The use of concentrated HF (49%) ensures a high etching selectivity between the oxide and metal layers in this process. A carefully controlled etching time and a quick blow of the etchant with nitrogen air before rinsing with water avoid the formation of  $\text{H}_3\text{O}^+$  and prevent any damage to the aluminum interconnects and the active device regions.<sup>[23]</sup> Another plasma etching step removes any oxide residues present near the device regions and exposes the multilayered “skeleton” of the electronic device. Next, spin casting of a liquid-form of silicone elastomer onto the top side of the device/IC, followed by a degassing process, uniformly fills and replaces the void regions of the multilayer. A room temperature curing process of silicone elastomer on a leveled surface creates a planar top surface and eliminates any mechanical stress created during the curing process, and a further heated annealing process fully cures the elastomer (**Figure 1c**). The elastic modulus ( $E$ ) of the replaced silicone elastomer ( $E = 2.6 \text{ MPa}$ )<sup>[24]</sup> compared to the original oxide layer ( $E = 80 \text{ GPa}$ )<sup>[25]</sup> is significantly lower, providing a mechanically relaxed environment for the devices and interconnects to deform without fracture. The difference in terms of dielectric permittivity ( $\epsilon$ ) in these two materials can alter the electrical performance, but the subtle difference in the replaced elastomer ( $\epsilon = 2.8$ )<sup>[26]</sup> compared to the original oxide ( $\epsilon = 3.9$ )<sup>[27]</sup> induces capacitance and inductance changes that have minor effects in the overall IC performance. The later section of this report compares the electrical performances of the original and transformed devices. The

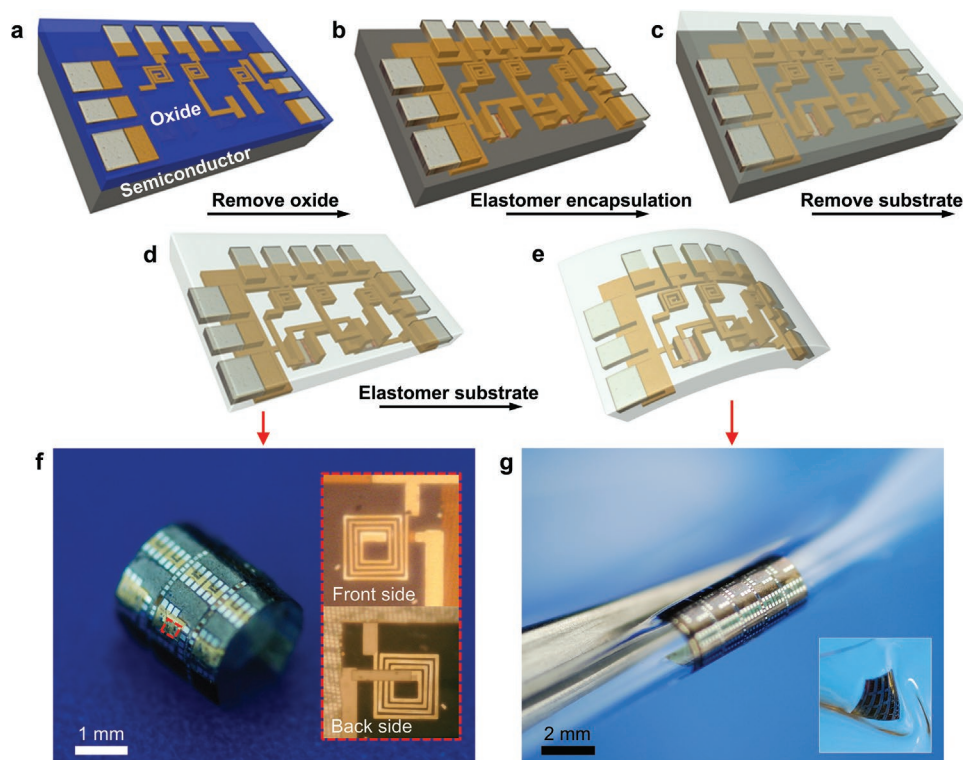


**Figure 1.** Microwave flexible electronics directly transformed from foundry-produced, multilayered MMIC. Schematic illustrations of steps for transforming a foundry-produced MMIC, including a) forming a device following conventional IC-fabrication strategies; b) removing the oxide layers in between the multilayered structure using combinations of wet and dry etchings; c) encapsulating and filling the voided regions of the multilayered structure with silicone elastomer; d) removing the original silicon substrate using combinations of wafer grinding and dry etching; e) coating the bottom of the IC to replace the original substrate with a silicone elastomer that matches the thickness of the top silicone to place mechanical neutral plane in the plane of the active IC. f) Image of the microwave IC after step (d), during the transformation process. g) Images of the finalized flexible microwave IC containing SiGe-based RF amplifier and individual HBTs. The main image shows the device folded with a radius of curvature of 3 mm and the inset shows the device in an unfolded state.

next step in the fabrication involves the removal of the rigid substrate. The device is attached to a temporary wafer using wax, which can be dissolved with acetone after the process is complete. A wafer backgrinding process removes most of the Si substrate, followed by a deep RIE procedure to remove the remaining Si ( $\approx 50 \mu\text{m}$ ). The etching rate slows down as Si is completely removed and the graded  $\text{Si}_{1-x}\text{Ge}_x$  layer of the chip is exposed, which acts as the optimal stopping point. The etch time depends on the thickness of the remaining silicon; the typical etching time is  $\approx 30$  min for  $\approx 50 \mu\text{m}$  of remaining silicon. A low power sulfur hexafluoride ( $\text{SF}_6$ )-based RIE process further removes the remaining graded  $\text{Si}_{1-x}\text{Ge}_x$  layer through a lithographically defined photoresist mask that protects the active device regions (Figure 1d). The process continues until the top silicone elastomer layer is exposed, which can be verified via visual inspection. Complete removal of the substrate prepares the device for spin casting another layer of silicone elastomer on the backside of the device (Figure 1e). Figure 1f shows a photographic image of the SiGe-based MMIC that is released from the temporary substrate after the bottom substrate removal process and just before coating the backside with a silicone elastomer. The device curls significantly due to the mechanical mismatch from silicone layer coating only on the top side. The backside coating thereby requires a temporary handling sub-

strate based on silicone adhesive to hold the flattened device. The thickness of coated elastomer substrate ( $100 \mu\text{m}$ ) matches the top elastomer layer to yield a neutral mechanical plane that defines the position in the layers where strain is zero, at the device/IC plane. The inset of Figure 1f shows a close-up look at the front and backside of an inductor, which is visible through the two sandwiching transparent elastomer layers. After the complete transformation (i.e., bottom silicone layer coating), the device remains mechanically stable and does not show any fractures upon bending with a small radius of curvature ( $r \approx 3$  mm), as appears in Figure 1g.

Figure 2a,b shows optical micrographs of the MMIC before and after the removal of the oxide layers. The removal process is a critical procedure because excessive exposures to plasma power and HF acid physically collapse the delicate structure of the “skeleton” and chemically degrades the materials. The goal is to remove IMD and ILD layers entirely without physical deformation of the “skeleton” and damage to the HBTs, capacitors, and inductors. The first RIE procedure minimizes the physical bombardment of  $\text{CF}_4$  ions to the surface with relatively low power and achieves partially isotropic etching to remove any exposed  $\text{SiO}_2$ . At a fixed RIE condition (10 mTorr pressure; 100 W power), the device measured after each 5 min etching cycle for a total of 45 min shows the negligible change

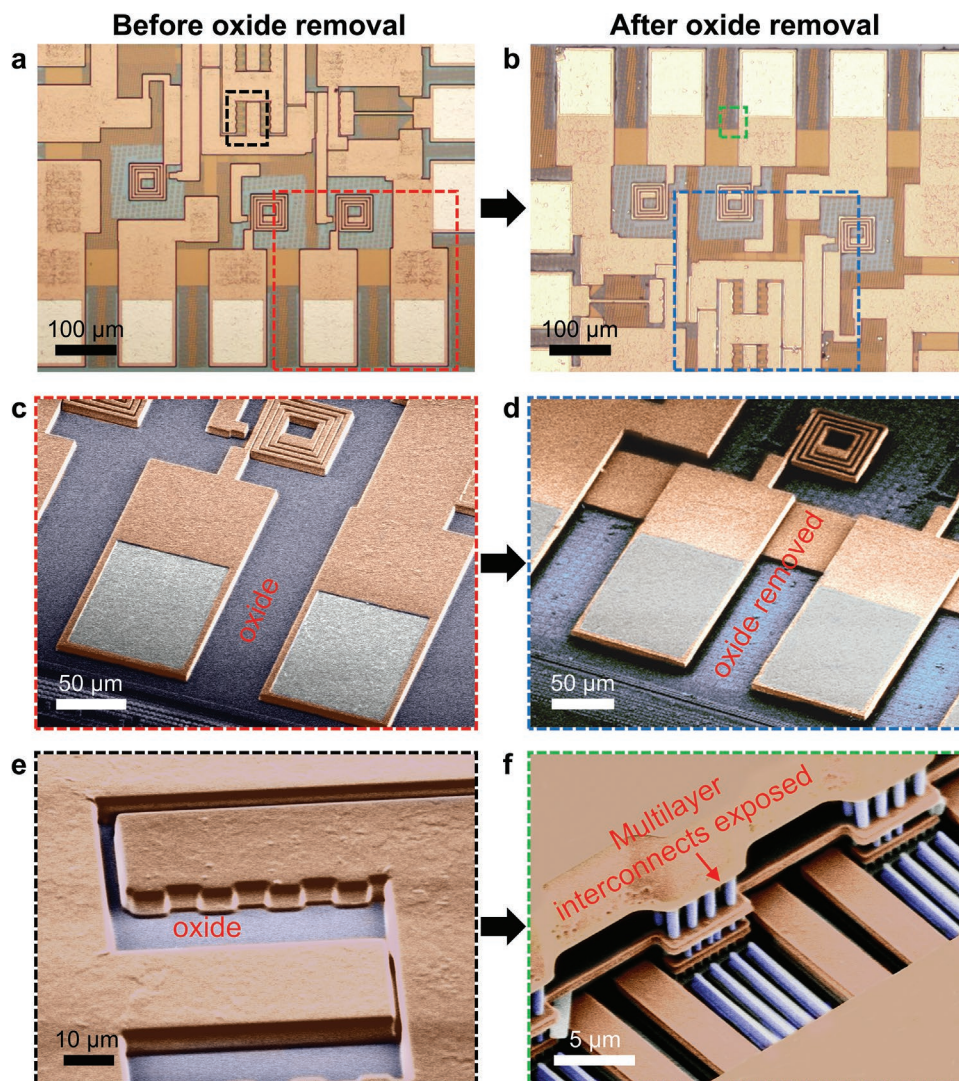


**Figure 2.** Sequence of images to illustrate the process of removing oxide-based dielectric layers in the foundry-produced MMIC. Optical micrographs showing the top side of the MMIC a) before and b) after the oxide removal process. SEM images showing close up views of the measurement pads and spiral inductors c) before and d) after the oxide removal process. SEM images showing close up views of the multilayer interconnects e) before and f) after the oxide removal process.

in high-frequency performance. A profilometer-based measurement of oxide thickness shows no further change in the etching depth after 15 min of RIE, indicating complete removal of the  $\text{SiO}_2$  that is visible from the top. An etching of 45 min also induced darkening of the metal surface under optical inspection, indicating a damaged surface induced by excessive RIE (Figure S1b, Supporting Information). The next HF-based wet etching procedure completely removes the  $\text{SiO}_2$  between the metal layers. Controlling the etching time is critical in this step as HF acid chemically attacks aluminum and forms a fluoride film resulting in a rough surface as well as via hole disconnections.<sup>[23]</sup> The  $\text{SiO}_2$  layer is partially removed at 10 s and completely removed at 25 s (Figure S1c, Supporting Information), and the device is fully functional at both stages. Scanning electron microscopy (SEM) images in Figure S2 (Supporting Information) confirms the removal of the  $\text{SiO}_2$ . At 40 s of HF exposure, the device is no longer operational as a

result of the collapsing of the metal structures on top of the HBTs that is observed under SEM inspection (Figure S3a, Supporting Information). Failure of the device can also arise from the physical degradation of the passive components, especially from the deformation of the spiral inductor. Specifically, the free-standing spiral inductor after etching of the surrounding  $\text{SiO}_2$  can deform the spiral shape, which typically occurs at the drying stage with strong nitrogen blow (Figure S3b, Supporting Information). Although the exposure to HF can etch the insulator ( $\text{Ta}_2\text{O}_5$ ) of the MIM-based capacitor, the large lateral dimension of the capacitor and a moderate etching selectivity of  $\text{Ta}_2\text{O}_5$  over  $\text{SiO}_2$  (1:5) in HF acid minimize the effect of capacitance change in device performance.<sup>[28]</sup> Figure 2c,d shows false-colored SEM images of the upper-level regions of the IC before and after the successful  $\text{SiO}_2$  removal process. Both the measurement pads and the inductor part of the device remain intact without deformation or sagging. A detailed view

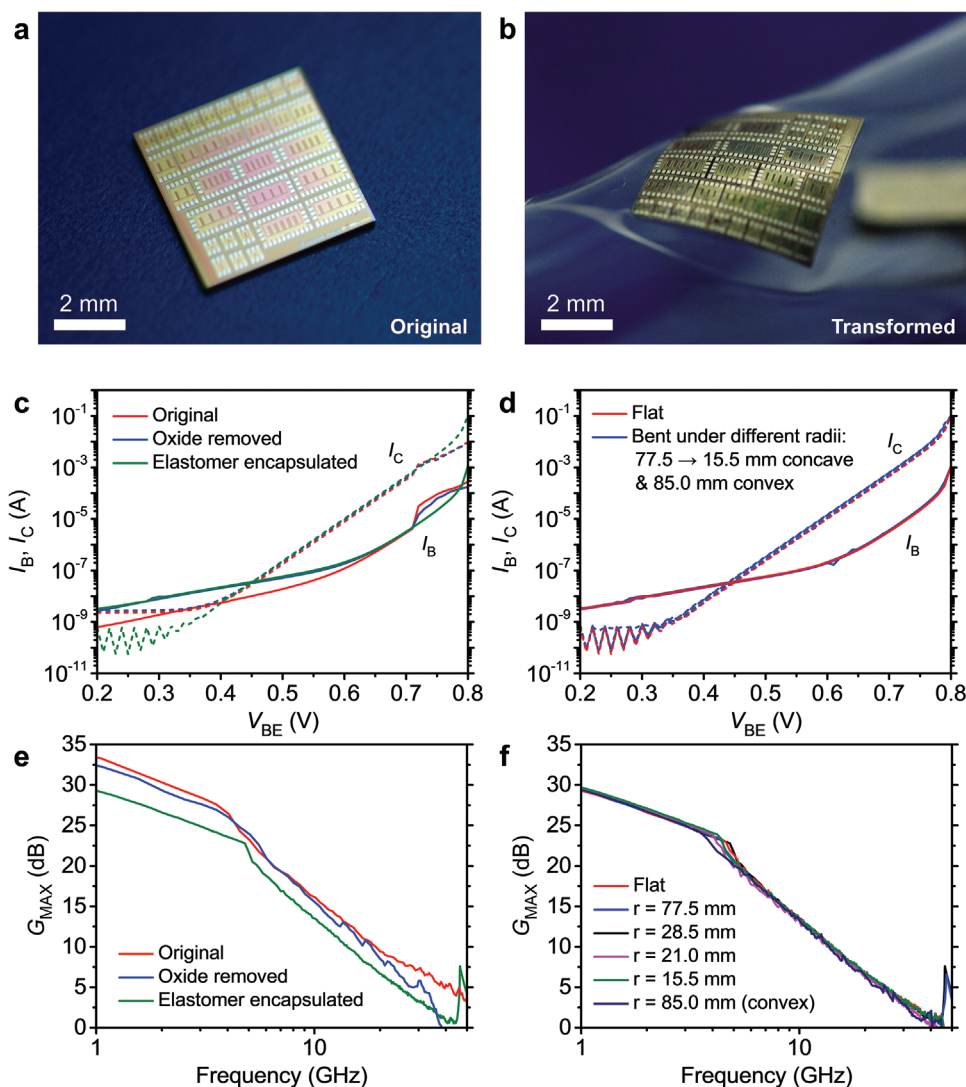


**Figure 3.** Foundry-produced SiGe HBTs transformed into a flexible format. Optical micrographs of an array of HBTs a) before and b) after the transformation process. c) Gummel plots of a single HBT subcell (four emitter fingers) in its original foundry-produced state, after the oxide removal process and after encapsulating the top surface with silicone elastomer. The plot shows the comparisons of collector current ( $I_C$ ; dashed lines) and base current ( $I_B$ ; solid lines), against base–emitter voltage ( $V_{BE}$ ) with zero base–collector voltage ( $V_{BC}$ ) bias. d) Gummel plots of a transformed single HBT subcell measured with equivalent conditions as in (c) and under various bending conditions. The red curve shows the measurement of the device in a flat state and the overlapping blue curves show the measurements under bending conditions (concave bending of 77.5, 28.5, 21.0, and 15.5 mm, and convex bending of 85.0 mm). e) Power gain as a function of frequency of the single HBT subcell in its original foundry-produced state, after the oxide removal process and after encapsulating the top surface with silicone elastomer. Collector bias is 2 V. f) Power gain of a transformed single HBT subcell measured with equivalent conditions as in (e) and under various bending conditions.

revealing the subcell region of the HBTs appears in Figure 2e (before) and 2f (after).

The individual HBTs that are present in the MMIC govern the overall performance of the circuit. Maintaining the high gain at high frequency without significant degradation is, thus, important. Critical aspects from the transformation process that can alter the direct current (DC) and RF performances of an HBT include the degradation of metal contacts due to etching and the changes in the dielectric environment due to the replacement of oxides with elastomers. A separate analysis of individual HBTs reveals the subtle changes in performance after transforming them into a flexible format. **Figure 3a,b** shows an array of HBTs with a different number of fingers

transformed from the original, foundry-produced state to an oxide-removed, elastomer-encapsulated state, respectively. The Gummel plot, which reflects the collector current ( $I_C$ ) and base current ( $I_B$ ), against base–emitter voltage ( $V_{BE}$ ) with zero base–collector voltage ( $V_{BC}$ ) bias, is shown in logarithmic scale in Figure 3c. Removing the oxides slightly increases the  $I_B$  at a  $V_{BE}$  range of 0.2–0.65 V and replacing the encapsulation with an elastomer does not recover the degraded base current. The increase in  $I_B$  observed at the oxide-removal stage arises from the degradation of base and emitter resistances from the HF acid etching procedure. Specifically, the HF acid etches the aluminum-based metal at a rate of  $\approx 40 \text{ nm min}^{-1}$ , reducing the area of the base and emitter metal contact regions that leads to

an increase in resistance. The decrease in  $I_C$  for the elastomer-encapsulated HBT at a  $V_{BE}$  range of 0.2–0.4 V arises from the decreased leakage current from exposure to HF acid that effectively reduces the surface recombination current. An encapsulation with a silicone elastomer that replaces the original oxide layers prevents further damage. Comparisons of the base and the collector current in the linear region of the plot, which is the region of interest for small-signal amplifier applications, reveal nearly identical behaviors at all stages of transformation. The transformed transistor shows a peak DC current gain ( $\beta$ ) of 150, as appears in the common-emitter current gain curve shown in Figure S4 (Supporting Information). Figure 3d shows the Gummel plots of the transformed HBT in a flat state (un-bent) and bent along the direction of the ground–signal–ground (G-S-G) measurement pads. The results show little or no changes in the DC characteristics for concave bending at radii of 77.5, 28.5, 21.0, and 15.5 mm, and convex bending at a radius of 85.0 mm. Specifically, the  $I_C$  fluctuates between 0.33 to 0.62 mA at  $V_{BE}$  of 0.7 V. RF measurements of the HBT at different stages made using a vector network analyzer over a frequency range of 0.045–50 GHz reveal the high-frequency characteristics. A calibration procedure to the probe tips using short-open-load-through (SOLT) standards on a calibration substrate as well as a de-embedding procedure that subtracts the effect of parasitic capacitances and inductances ensure accurate electrical characteristics of the HBT. Figure 3e presents the maximum available gain derived from the S-parameters at a bias of  $V_{CE} = 2$  V. Here, the results indicate a maximum oscillation frequency ( $f_{max}$ ) of 73 GHz at the original, foundry-produced state.

After the oxide-removal,  $f_{max}$  decreases to 55 GHz and after elastomer-encapsulation,  $f_{max}$  further decreases to 49 GHz. The available gains at 24 GHz, which is the frequency of interest, are 8.2, 6.8, and 5.2 dB at the original, after the oxide-removal and after elastomer-encapsulation states, respectively. Despite such degradations, the gain of the HBT remains stable at different mechanical bending radii, fluctuating between 4.6 and 5.2 dB at 24 GHz, as appears in Figure 3f.

A transformed small-signal amplifier further verifies the effectiveness of this approach in generating a high-performance microwave IC in a flexible format. Specifically, the two-stage 24 GHz amplifier transformed from an original, foundry-produced state into an elastomer-filled, substrate-replaced state shows an insignificant change in its high-frequency characteristics. Figure 4a,b shows optical images of the transformed amplifier from the top and backside, respectively. Clearly visible spiral inductors from the backside indicate a fully removed original substrate that is replaced with a transparent silicone elastomer. The backside image in Figure 4b also shows the SiGe-based active layer of individual HBTs that has been protected with a photoresist mask to prevent from being damaged during the last RIE-based etching step. The details of the small-signal amplifier are shown in Figure S5 (Supporting Information) showing that the amplifier consists of a common-emitter configuration in the first stage and a common-base configuration in the second stage. The inductors and capacitors serve as baluns at different stages of the IC to provide optimized microwave ground for the amplifiers and impedance-matched connections in between the input, the

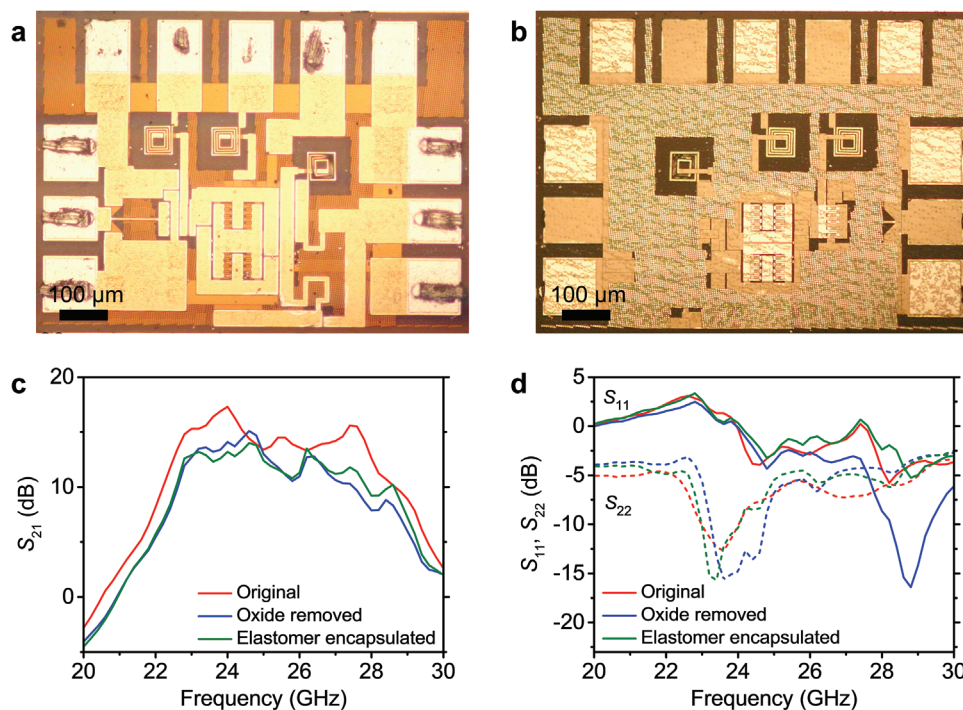


**Figure 4.** A 24 GHz small-signal amplifier transformed into a flexible format. a) Top view and b) bottom view optical micrographs of the transformed amplifier. c) Measured small-signal gain ( $S_{21}$ ) plots under equivalent output DC current at different stages of the transformation process (original, after oxide removal and after encapsulation) for the frequency range of 20 to 30 GHz. d) Input ( $S_{11}$ ; solid lines) and output ( $S_{22}$ ; dashed lines) matching conditions at different stages of the transformation process.

**Table 1.** Examples of flexible microwave amplifiers organized according to their technologies, and performance attributes.

Type	Key features	Transistor technology	Operating frequency [GHz]	Peak small-signal gain [dB]	Bending Radius [mm]	Reference
Power amplifier (PA)	Fabricated on cellulose nanofibril substrate	GaN HEMT	5.3	6.69	28.5	[18]
	Three-path BiCMOS PA on thinned substrate	SiGe BiCMOS	5.5	9.7	–	[29]
Low-noise amplifier (LNA)	Three-path BiCMOS LNA on thinned substrate	SiGe BiCMOS	6.3	11.6	–	[30]
	W-band mm-wave flexible LNA	InP HEMT	100	10	–	[31]
Small-signal amplifier	Transformed from foundry-produced MMIC	SiGe HBT	24	13.2	15.5	This work

output, and the HBTs. Figure 4c shows the small-signal gain based on measured scattering (S)-parameters of the amplifier at various stages of the transformation process, under equivalent DC bias conditions ( $V_{B1} = V_{B2} = 0.87$  V,  $V_{C1} = 2$  V,  $V_{C2} = 3.85$  V). The amplifier, in its original, foundry-produced state, exhibits 17.3 dB of gain ( $S_{21}$ ) at 24 GHz, that changes to 14.1 dB after the oxide-removal process and to 13.2 dB after the silicone elastomer-based encapsulation process. The degradations in the gains of 4.1 dB arise presumably due to the comprehensive subtle damages in the HBTs from HF acid exposure as related to the discussion in the previous section of this report based on individual HBT analysis. The matching conditions of the amplifier ( $S_{11}$  and  $S_{22}$ ) exhibit significant changes after the oxide is removed, due to the exposure of the components and transmission lines to air ( $\epsilon = 1.0$ ), as shown in Figure 4d. The matching conditions, however, return closely to their original conditions after the transformation is completed. Specifically, the input matching point of the circuit slightly shifts to a lower frequency ( $\approx 23.4$  GHz), due to the change in the dielectric medium from  $\text{SiO}_2$  ( $\epsilon = 3.9$ ) to silicone elastomer ( $\epsilon = 2.8$ ). The  $S_{22}$  of the transformed amplifier, nevertheless, is  $-10.4$  dB at 24 GHz, which indicates a sufficient matching condition for high-frequency applications. The transformed amplifier could not be analyzed under bending, due to the perpendicular alignment of the measurement pads in the IC design that prevents probing the device along the bent side with a microwave G-S-G probe consisting of parallel probing tips designed to contact with pads on a flat surface. Under bending conditions, however, negligible performance changes from the measurements at the elastomer-encapsulated stage in Figure 4c,d can be assumed, as the analysis in Figure 3 clearly indicates that the degradation mostly occurs during the transformation process and bending of the device induces a negligible change in the overall DC and RF performances in the HBT. Moreover, a stability test indicates a stable, flexible microwave amplifier that can withstand more than 1000 cycles of bending, as appears in Figure S6 (Supporting Information). Although the changes in the gains and the operating frequency clearly indicate a mild degradation in performance during the transformation procedure, the results reported here represent a flexible microwave amplifier with a small-signal gain that is higher than 10 dB at such a high frequency ( $>20$  GHz). Table 1 summarizes examples of flexible microwave amplifiers, organized according to their key technologies and performance attributes.<sup>[18,29–31]</sup>

### 3. Conclusion

The materials and fabrication strategies presented here demonstrate the capability of transforming foundry-produced, high-performance, rigid inorganic semiconductor-based ICs into those with mechanically compliant properties. Replacing most of the brittle materials that do not need to provide any active electronic functionality (i.e., dielectric and substrate) with soft and flexible elastomers is the key to this approach. These results represent important steps toward flexible ICs because existing bottom-up approaches are not suitable for the fabrication of ICs with levels of performance that are valuable for circuit implementations. The strategies introduced here could extend to nearly all conventional ICs based on Si into flexible formats with modified protocols, for example, using methods that prevent the etching of oxides in a complementary metal-oxide-semiconductor. The remaining technical improvements include the search for soft dielectric materials with electrical characteristics (i.e., permittivity) that are similar to those with original dielectric materials in order to prevent significant changes in the overall performance of the IC. Exploring devices based on other material systems, such as gallium nitride MMICs based on high electron mobility transistors and gallium arsenide MMICs based on HBTs represent promising directions for future work.

### 4. Experimental Section

*Fabrication of Flexible HBTs and Small-Signal Amplifier:* The individual HBTs and small-signal amplifier IC on bulk Si pieces (5 mm  $\times$  5 mm) were first subject to dry etching (Unaxis 790;  $\text{CF}_4 = 10$  sccm, pressure = 10 mTorr, power = 100 W) for 15 min, followed by exposure to highly concentrated (49%) HF for 25 s to remove the  $\text{SiO}_2$  layers. A liquid form of poly(dimethylsiloxane) (PDMS; Sylgard 184, Dow Corning; 10:1 mixture of pre-polymer to curing agent) was spin coated at 1200 rpm for 5 min onto the front side of the device/IC to uniformly fill in the empty space, followed by a room temperature curing for 24 h on a leveled surface. The PDMS layer was further cured at 80 °C for 4 h in an oven. The front side of the device/IC was glued to a handling Si wafer using wax and the backside was grinded to reach a total wafer thickness of 50  $\mu\text{m}$  (Grinding and Dicing Services Inc.). Dry etching using an inductively coupled plasma (ICP) RIE (STS Multiplex; 124 cycles of etch:  $\text{SF}_6/\text{O}_2 = 101/13$  sccm, plasma power = 11.7 W, ICP power = 600 W, time = 10.5 s, passivation:  $\text{C}_4\text{F}_8 = 97$  sccm, time = 6 s) was conducted to further remove the backside Si. The device (i.e., HBT) region of the device/IC was protected using a thick layer (12  $\mu\text{m}$ ) of photoresist mask (AZ P4620, AZ Electronic Materials), followed by a plasma dry etching process ( $\text{SF}_6 = 42$  sccm,  $\text{O}_2 = 5$  sccm,

pressure = 8 mTorr, power = 50 W) to fully remove the backside SiGe layer. The photoresist layer was removed using a quick blow of acetone, which prevents the removal of wax. A layer of liquid-form PDMS was spin coated to the backside using the same parameters and curing conditions as those applied to the front-side, such that the thickness of the two PDMS layers were the same on both sides. The device/IC was immersed in acetone to dissolve the wax and to detach the handling substrate.

**Measurement and Analysis:** A LEO Gemini 1530 Field Emission SEM was used to evaluate the etching process using images. The DC characteristics were measured using an Agilent 4155B semiconductor parameter analyzer. The 50 GHz ground-signal-ground (GSG) Cascade probes were used for the input and output signals. Picoprobe multi-contact GSGSG probe was used for extra grounding and for providing DC bias on the 24 GHz small-signal amplifier. An Agilent E8346A parameter network analyzer was employed for the RF measurement and was calibrated from 45 MHz to 50 GHz. An Agilent E3631A power supply was used to provide the DC power for the small-signal amplifier. Thickness of sample layers was measured using a Tencor Alphastep 200 profilometer. Samples were mounted on curvature modes with different radii (convex 77.5, 28.5, 21, and 15.5 mm, and concave 85 mm) for the measurement of the device/IC under bending conditions.

## Supporting Information

Supporting Information is available from the Wiley Online Library or from the author.

## Acknowledgements

G.Q. and Y.H.J. contributed equally to this work. This work was supported by the Air Force Office of Scientific Research (AFOSR): Presidential Early Career Award in Science & Engineering (PECASE) grant # FA9550-09-1-0482. The program manager was Dr. Gernot Pomrenke. This work was supported by the research fund of Hanyang University (HY-202100000003286). This work was supported by the Basic Science Research Program (NRF-2021R1F1A1061973) through the National Research Foundation of Korea funded by the Ministry of Science and ICT.

## Conflict of Interest

The authors declare no conflict of interest.

## Data Availability Statement

Research data are not shared.

## Keywords

flexible electronics, flexible integrated circuit, heterojunction bipolar transistor, monolithic microwave integrated circuit, small-signal amplifier

Received: December 12, 2021  
Revised: January 6, 2022  
Published online:

- [1] D. C. Kim, H. Yun, J. Kim, H. Seung, W. S. Yu, J. H. Koo, J. Yang, J. H. Kim, T. Hyeon, D.-H. Kim, *Nat. Electron.* **2021**, 4, 671.
- [2] X. Shi, Y. Zuo, P. Zhai, J. Shen, Y. Yang, Z. Gao, M. Liao, J. Wu, J. Wang, X. Xu, Q. Tong, B. Zhang, B. Wang, X. Sun, L. Zhang, Q. Pei, D. Jin, P. Chen, H. Peng, *Nature* **2021**, 591, 240.
- [3] M. Han, L. Chen, K. Aras, C. Liang, X. Chen, H. Zhao, K. Li, N. R. Faye, B. Sun, J.-H. Kim, W. Bai, Q. Yang, Y. Ma, W. Lu, E. Song, J. M. Baek, Y. Lee, C. Liu, J. B. Model, G. Yang, R. Ghaffari, Y. Huang, I. R. Efimov, J. A. Rogers, *Nat. Biomed. Eng.* **2020**, 4, 997.

- [4] Y. Yang, M. Wu, A. Vázquez-Guardado, A. J. Wegener, J. G. Grajales-Reyes, Y. Deng, T. Wang, R. Avila, J. A. Moreno, S. Minkowicz, V. Dumrongprechachan, J. Lee, S. Zhang, A. A. Legaria, Y. Ma, S. Mehta, D. Franklin, L. Hartman, W. Bai, M. Han, H. Zhao, W. Lu, Y. Yu, X. Sheng, A. Banks, X. Yu, Z. R. Donaldson, R. W. Gereau, C. H. Good, Z. Xie, et al., *Nat. Neurosci.* **2021**, 24, 1035.
- [5] Z. Rao, Y. Lu, Z. Li, K. Sim, Z. Ma, J. Xiao, C. Yu, *Nat. Electron.* **2021**, 4, 513.
- [6] K. Zhang, Y. H. Jung, S. Mikael, J.-H. Seo, M. Kim, H. Mi, H. Zhou, Z. Xia, W. Zhou, S. Gong, Z. Ma, *Nat. Commun.* **2017**, 8, 1782.
- [7] D. M. Pozar, *Microwave and RF design of wireless systems*, John Wiley & Sons, Hoboken, NJ, USA **2000**.
- [8] Y. Zhan, Y. Mei, L. Zheng, *J. Mater. Chem. C* **2014**, 2, 1220.
- [9] S. Xu, Y. Zhang, L. Jia, K. E. Mathewson, K. - I. Jang, J. Kim, H. Fu, X. Huang, P. Chava, R. Wang, S. Bhole, L. Wang, Y. J. Na, Y. Guan, M. Flavin, Z. Han, Y. Huang, J. A. Rogers, *Science* **2014**, 344, 70.
- [10] K. Lee, X. Ni, J. Y. Lee, H. Arafa, D. J. Pe, S. Xu, R. Avila, M. Irie, J. H. Lee, R. L. Easterlin, D. H. Kim, H. U. Chung, O. O. Olabisi, S. Getaneh, E. Chung, M. Hill, J. Bell, H. Jang, C. Liu, J. B. Park, J. Kim, S. B. Kim, S. Mehta, M. Pharr, A. Tzavelis, J. T. Reeder, I. Huang, Y. Deng, Z. Xie, C. R. Davies, et al., *Nat. Biomed. Eng.* **2020**, 4, 148.
- [11] Y. H. Jung, H. Zhang, S. J. Cho, Z. Ma, *IEEE Trans. Electron Devices* **2017**, 64, 1881.
- [12] H. Zhang, Y. Lan, S. Qiu, S. Min, H. Jang, J. Park, S. Gong, Z. Ma, *Adv. Mater. Technol.* **2021**, 6, 2000759.
- [13] J. Lewis, *Mater. Today* **2006**, 9, 38.
- [14] X. Zhang, J. Grajal, J. L. Vazquez-Roy, U. Radhakrishna, X. Wang, W. Chern, L. Zhou, Y. Lin, P.-C. Shen, X. Ji, X. Ling, A. Zubair, Y. Zhang, H. Wang, M. Dubey, J. Kong, M. Dresselhaus, T. Palacios, *Nature* **2019**, 566, 368.
- [15] L. Sun, G. Qin, J.-H. Seo, G. K. Celler, W. Zhou, Z. Ma, *Small* **2010**, 6, 2553.
- [16] H.-J. Chung, T.-i. Kim, H.-S. Kim, S. A. Wells, S. Jo, N. Ahmed, Y. H. Jung, S. M. Won, C. A. Bower, J. A. Rogers, *Adv. Funct. Mater.* **2011**, 21, 3029.
- [17] J.-K. Chang, H. Fang, C. A. Bower, E. Song, X. Yu, J. A. Rogers, *Proc. Natl. Acad. Sci. U.S.A.* **2017**, 114, E5522.
- [18] H. Zhang, J. Li, D. Liu, S. Min, T.-H. Chang, K. Xiong, S. H. Park, J. Kim, Y. H. Jung, J. Park, J. Lee, J. Han, L. Katehi, Z. Cai, S. Gong, Z. Ma, *Nat. Commun.* **2020**, 11, 3118.
- [19] I. D. Robertson, S. Lucyszyn, *RFIC and MMIC Design and Technology*, The Institution of Electrical Engineers, London, **2001**.
- [20] Y. Zhai, L. Mathew, R. Rao, D. Xu, S. K. Banerjee, *Nano Lett.* **2012**, 12, 5609.
- [21] S. Gupta, W. T. Navaraj, L. Lorenzelli, R. Dahiya, *npj Flex. Electron* **2018**, 2, 8.
- [22] C.-W. Cheng, K.-T. Shiu, N. Li, S.-J. Han, L. Shi, D. K. Sadana, *Nat. Commun.* **2013**, 4, 1577.
- [23] J. Bühler, F. P. Steiner, H. Baltes, *J. Micromech. Microeng.* **1997**, 7, R1.
- [24] Z. Wang, A. A. Volinsky, N. D. Gallant, *J. Appl. Polym. Sci.* **2014**, 131.
- [25] H. Ni, X. Li, H. Gao, *Appl. Phys. Lett.* **2006**, 88, 043108.
- [26] N. J. Farcich, J. Salonen, P. M. Asbeck, *IEEE Trans. Microw. Theory Tech.* **2008**, 56, 2963.
- [27] J. Robertson, *EPJ Appl. Phys.* **2004**, 28, 265.
- [28] C. Christensen, R. d. Reus, S. Bouwstra, *J. Micromech. Microeng.* **1999**, 9, 13.
- [29] S. Özbek, G. Alavi, J. Digel, M. Grözing, J. N. Burghartz, M. Berroth, *Integration* **2018**, 63, 291.
- [30] S. Özbek, M. Grözing, G. Alavi, J. N. Burghartz, M. Berroth, presented at *48th European Microwave Conference (EuMC)*, Madrid, Spain, **2018**.
- [31] H. Sharifi, J. May, K. Shinohara, M. Montes, C. McGuire, H. Kazemi, presented at *2013 IEEE MTT-S International Microwave Symposium*, Seattle, WA, USA, **2013**.